







## Origin and control of ionic hydration patterns in nanopores

Miraslau L. Barabash <sup>1</sup>✉, William A. T. Gibby <sup>1</sup>, Carlo Guardiani <sup>1,3</sup>, Alex Smolyanitsky <sup>2</sup>, Dmitry G. Luchinsky <sup>1,4</sup> & Peter V. E. McClintock <sup>1</sup>

In order to permeate a nanopore, an ion must overcome a dehydration energy barrier caused by the redistribution of surrounding water molecules. The redistribution is inhomogeneous, anisotropic and strongly position-dependent, resulting in complex patterns that are routinely observed in molecular dynamics simulations. Here, we study the physical origin of these patterns and of how they can be predicted and controlled. We introduce an analytic model able to predict the patterns in a graphene nanopore in terms of experimentally accessible radial distribution functions, giving results that agree well with molecular dynamics simulations. The patterns are attributable to a complex interplay of ionic hydration shells with water layers adjacent to the graphene membrane and with the hydration cloud of the nanopore rim atoms, and we discuss ways of controlling them. Our findings pave the way to designing required transport properties into nanoionic devices by optimising the structure of the hydration patterns.

<sup>1</sup>Department of Physics, Lancaster University, Lancaster, UK. <sup>2</sup>Applied Chemicals and Materials Division, National Institute of Standards and Technology, Boulder, CO, USA. <sup>3</sup>Present address: Department of Mechanical and Aerospace Engineering, Sapienza University, Rome, Italy. <sup>4</sup>Present address: KBR Inc., Ames Research Center, Moffett Field, CA, USA. ✉email: [miroslav.barabash@gmail.com](mailto:miroslav.barabash@gmail.com)

Ionic permeation through narrow water-filled channels and pores is of profound importance in both biophysics and technology<sup>1,2</sup>, finding applications in fuel cells<sup>3</sup>, biological ion channels<sup>4</sup>, water desalination<sup>5–8</sup>, gas<sup>9</sup> and isotope<sup>10</sup> separation, DNA sequencing<sup>11,12</sup>, and “blue energy” harvesting<sup>12–14</sup>. Angstrom-sized pores in artificially fabricated membranes are promising candidates for reproducible on-demand engineering and control of selective ionic and molecular transport.

It is well-known that the structure of ionic hydration shells is one of the key factors controlling ionic permeation in nanopores<sup>8,15–17</sup>. In confined geometries, some of the water molecules are lost from the hydration shells, and the resultant dehydration barrier is the subject of extensive research<sup>8,17–28</sup>. One outcome is an appreciation of the extraordinary complexity of the hydration patterns around an ion in the pore<sup>18,22,29</sup>, as has been confirmed by numerous molecular dynamics (MD) simulations<sup>5,8,22,30,31</sup>. The latter reveals that the patterns are highly inhomogeneous, anisotropic and spatially clustered near membranes<sup>32</sup>, inside nanotubes<sup>33</sup>, and in nanoslits<sup>16,34</sup>. This clustering determines the distribution of charge around the ion, the local dielectric permittivity<sup>35,36</sup>, and the strength of the ions’ electrostatic interactions with their surroundings<sup>37</sup>. However, to understand, characterise, and predict the hydration patterns theoretically is a challenging problem<sup>2</sup> that hitherto has remained unresolved.

We now develop an analytic model that can predict the hydration patterns of ions in nano-confinement through the use of radial distribution functions (RDFs), evaluated in the bulk electrolyte. We show that the patterns result from interference between the ionic hydration shells, water layering near the membranes, and the hydration cloud around the nanopore. We compare the analytically predicted patterns with the results of MD simulations for different ionic locations near graphene nanopores with a diversity of shapes, geometries and strains. The results are applicable to narrow biological channels<sup>24,38,39</sup>, functionalised sub-nanopores<sup>24,25,40,41</sup>, nanotubes<sup>42</sup> and nanoslits<sup>16,34</sup>. Thus, this work takes an important step towards controlling the function of nanoscale devices by tailoring the hydration patterns.

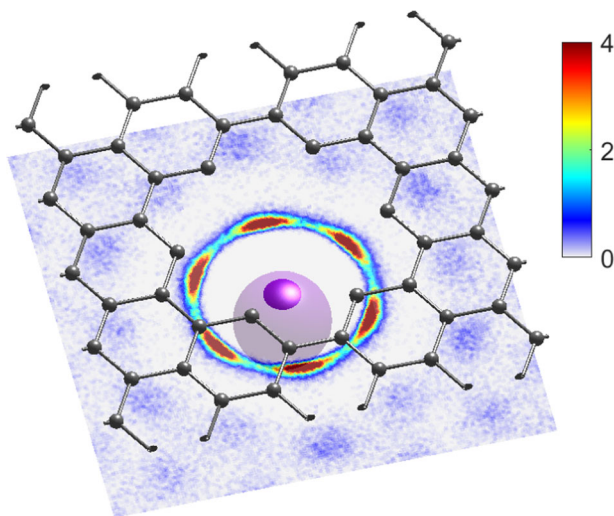


**Fig. 1 Model setup.** A hexagonal pore in pristine graphene (grey balls and sticks) and a  $K^+$  ion (purple sphere) centred at  $Z = -0.4$  nm. The colour plane represents the density pattern of water oxygen atoms in the plane at  $Z = -0.28$  nm. (There will be comparable colour planes at other  $Z$  values.) The colours indicate density values relative to the bulk, brown being the highest (4) and dark blue being the lowest (0) value. The density has been evaluated by MD simulation, and it is compared with theory, Eq. (4), in Supplementary Fig. 1.

## Results

**Model.** We consider graphene lattice<sup>43</sup> with nanopore and an ion (e.g.  $K^+$ ) in a water box (see Fig. 1). The pore is created by removing one hexagon of carbon atoms from near the geometrical centre of the lattice.

For simplicity, we consider the carbons and the ion as being clamped. The spatial distribution of water oxygens is given by

$$\rho(\mathbf{r}_1^w | \{\mathbf{r}_m^c\}, \mathbf{r}^i) = \frac{1}{Z} \int \dots \int e^{-\beta H(\mathbf{r}_1^w, \dots, \mathbf{r}_{N_w}^w, \mathbf{p}_1^w, \dots, \mathbf{p}_{N_w}^w | \{\mathbf{r}_m^c\}, \mathbf{r}^i)} \times d\mathbf{r}_2^w \dots d\mathbf{r}_{N_w}^w d\mathbf{p}_1^w \dots d\mathbf{p}_{N_w}^w \quad (1)$$

where  $H(\cdot)$  is the all-atom Hamiltonian, comprising the water–ion  $U_{iw}$ , water–lattice  $U_{ic}$  and water–water  $U_{ww}$  interactions;  $Z$  is the partition function,  $\beta = 1/k_B T$ ,  $k_B$  is Boltzmann’s constant and  $T$  is the absolute temperature. Integration over momenta  $\mathbf{p}_n^w$  leads to a factor that subsequently cancels out due to normalisation. Here  $\{\mathbf{r}_n^w\}$ ,  $\{\mathbf{r}_m^c\}$ ,  $\mathbf{r}^i$  represent the 3D coordinates of the water molecules, atoms of the lattice, and the ion, respectively. Water molecules can be chosen arbitrarily, and so we omit the sub-index in  $\mathbf{r}_1$  for clarity, so that  $\mathbf{r}$  is used hereafter. Supplementary Discussions 1 and 2 in Supplementary Methods provide a more detailed derivation of the quantities in this section.

Direct application of the analytic formula (1) is not feasible due to a large number of degrees of freedom in the solution. However, statistical averaging over all water molecules generates rigorously the potential of the mean force (PMF)<sup>44–46</sup> which can be approximated as<sup>47,p. 77</sup>

$$W(\mathbf{r} | \{\mathbf{r}_m^c\}, \mathbf{r}^i) = \mathcal{W}_{iw}(\mathbf{r} - \mathbf{r}^i) + \sum_m^{N_c} \mathcal{W}_{cw}(\mathbf{r} - \mathbf{r}_m^c). \quad (2)$$

Note that the interactions of the ion or carbon atoms with other water molecules are already incorporated implicitly within the PMF. Note also that a similar strategy—construction of a multi-ion PMF from spherically symmetrical pairwise components measured in separate MD simulations—has been used successfully in an atomic-resolution Brownian dynamics study of the ionic selectivity of  $\alpha$ -Hemolysin<sup>48</sup> and to describe DNA translocation through nanopores<sup>49</sup>.

Importantly, the water PMF is related rigorously to the correlation function  $\mathcal{W}$  (CF) via<sup>44–46</sup>

$$\mathcal{W}(\mathbf{r}) = -\beta^{-1} \ln g(\mathbf{r}), \quad (3)$$

assuming that  $\mathcal{W} \rightarrow 0$  and  $g(\mathbf{r}) \rightarrow 1$  as  $\mathbf{r} \rightarrow \infty$ . We evaluate the RDFs in bulk through separate MD simulations (see Discussions 1 and 2 of Supplementary Methods for details). Note that this needs to be done only once for a given density  $\rho_0$  and temperature  $T^{50}$ .

The relations (2) and (3) allow one to rewrite the water spatial density  $\rho(\mathbf{r})$  in the form

$$\frac{\rho(\mathbf{r} | \{\mathbf{r}_m^c\}, \mathbf{r}^i)}{\rho_0} = g_{iw}(|\mathbf{r} - \mathbf{r}^i|) \cdot \prod_m^{N_c} g_{cw}(|\mathbf{r} - \mathbf{r}_m^c|). \quad (4)$$

where  $\rho_0$  is the bulk water density (see Supplementary Discussion 1 for details). Note that the modulus sign reduces the 3D ion–water and carbon–water interactions to ion–oxygen and carbon–oxygen interactions, respectively. Thus, one is relying on the radial density functions (RDFs)  $g(r)$  which are one-dimensional functions of distance, in contrast to three-dimensional CFs.

In the derivation, we take no explicit account of water–water interactions, in particular between their oxygen atoms. This simplification leads to the water being represented as an ideal gas, and it overestimates the water density near the graphene walls.

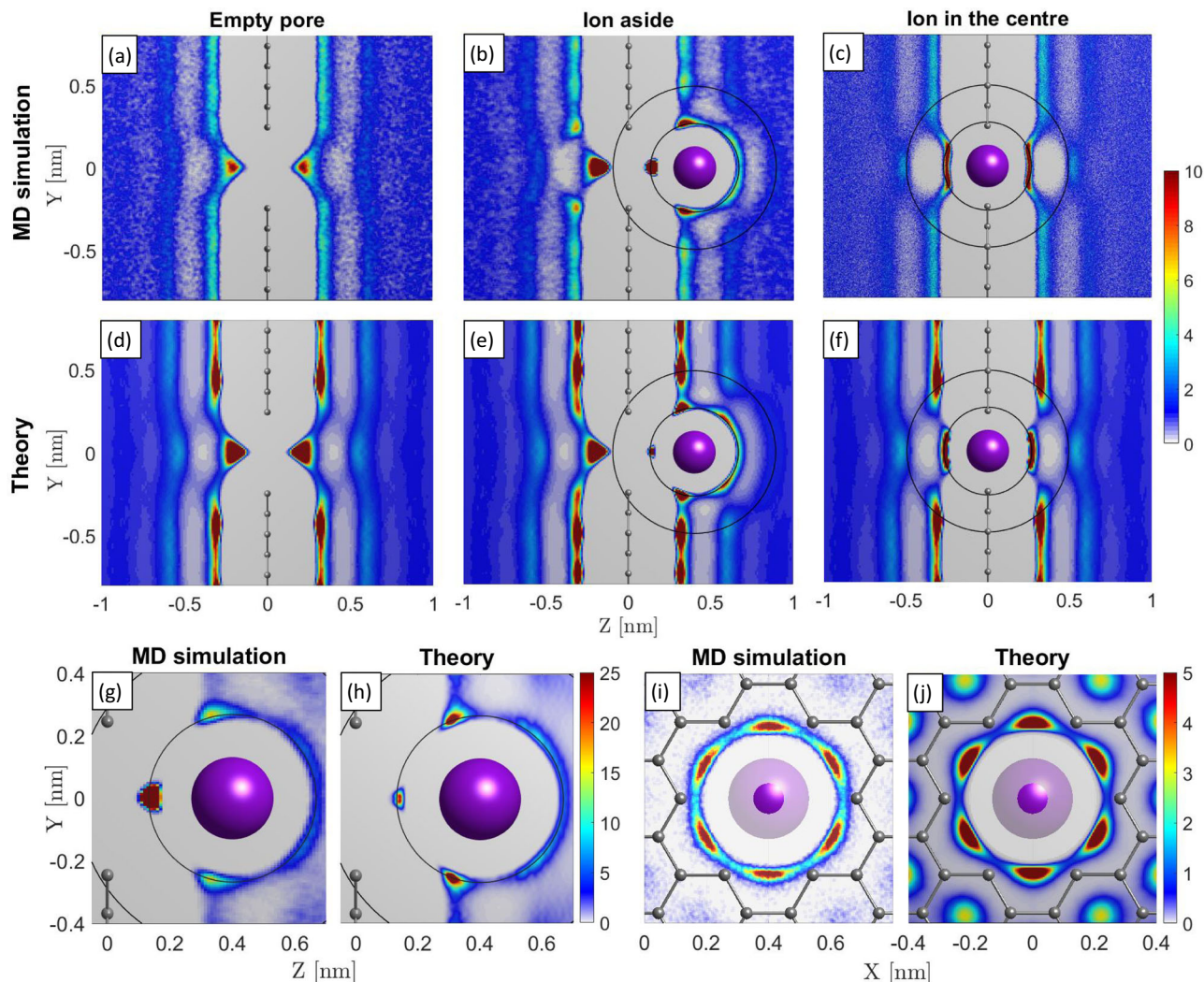


**Fig. 2 Comparison of analytic theory with MD simulations.** The graphene sheet is shown in section by the vertical line of carbon atoms, in which the pore appears as a centrally placed gap with the horizontal axis of symmetry. The  $O^-$  density in the vicinity of an ion (purple sphere) near the pore, derived from the MD simulations (a)–(c) is compared with the predictions of Eq. (4) (d)–(f). Panels a and d show the oxygen density around an empty pore; c and f show the density for a  $K^+$  ion in the centre of the pore; b and e show the density when the ion is centred 0.4 nm from the entrance to the pore. The fine structure of the oxygen density pattern around a  $K^+$  ion at the pore centre, obtained from MD simulations (g), (i) and from theory Eq. (4) (h), (j). The concentric black circles represent the first two maxima of the  $K^+-O^-$  RDF, and are given as guides to the eye. The graphene lattice is indicated in a grey ball-and-stick representation.

This can clearly be seen near the graphene lattice in the lower panels of Fig. 2.

Equation (4) allows one to compute the density of the water wetting a given set of atoms as a product of component RDFs, and to evaluate the water PMF via the Boltzmann inversion (3). Equation (4) also shows that the water pattern results from interference between the ionic hydration shells ( $g_{iw}$  term) and the water layers surrounding the graphene membrane ( $\Pi g_{cw}$  term). Supplementary Discussion 3 illustrates the emergence of the hydration pattern when groups of carbon atoms are added sequentially to compose a nanopore. Equation (4) represents the well-known Kirkwood superposition approximation<sup>50–52,p.186</sup>. It has also been generalised to describe the ice–water interface<sup>50</sup> and solvated DNA<sup>53</sup>. Here, we apply this relation for the first time to describe the water density patterns around an ion near an artificial nanopore.

The usefulness of an approach based on Eq. (4) is twofold. First, the use of the bulk RDF values to describe water density near the pore provides for a  $10^2$ – $10^4$  speed-up in comparison with all-atom MD simulations<sup>50</sup>. In turn, the single-component

bulk RDFs  $g(r)$  can be obtained in a number of ways. The most straightforward is to use experimental values derived from the structure factor measured by X-ray<sup>54</sup> or neutron<sup>55</sup> diffraction. Thus one can avoid uncertainties related to the properties of the force field (parametrisation, polarisability) and thus connect the experimentally measurable structural properties of the bulk electrolyte solution with those near a nanopore. Other approaches rely on MD, Monte-Carlo or DFT simulations, or on the integral theory of liquids<sup>46,56–59</sup>. In the present work, MD-derived RDFs have been chosen in order to simplify the comparison between the MD simulations and analytics.

Secondly, the method can be readily extended to any material or pore geometry. The latter paves the way towards changing the pore parameters—size, shape, number of layers, strain tensor, rim charge, functional groups and choice of lattice type (e.g.  $MoS_2$ , hBN,  $WS_2$ , etc. as well as graphene)—with the purpose of changing the dehydration pattern. The pattern defines the dehydration energy profile and thus determines the pore’s permeability and selectivity, which are vital for inverse-

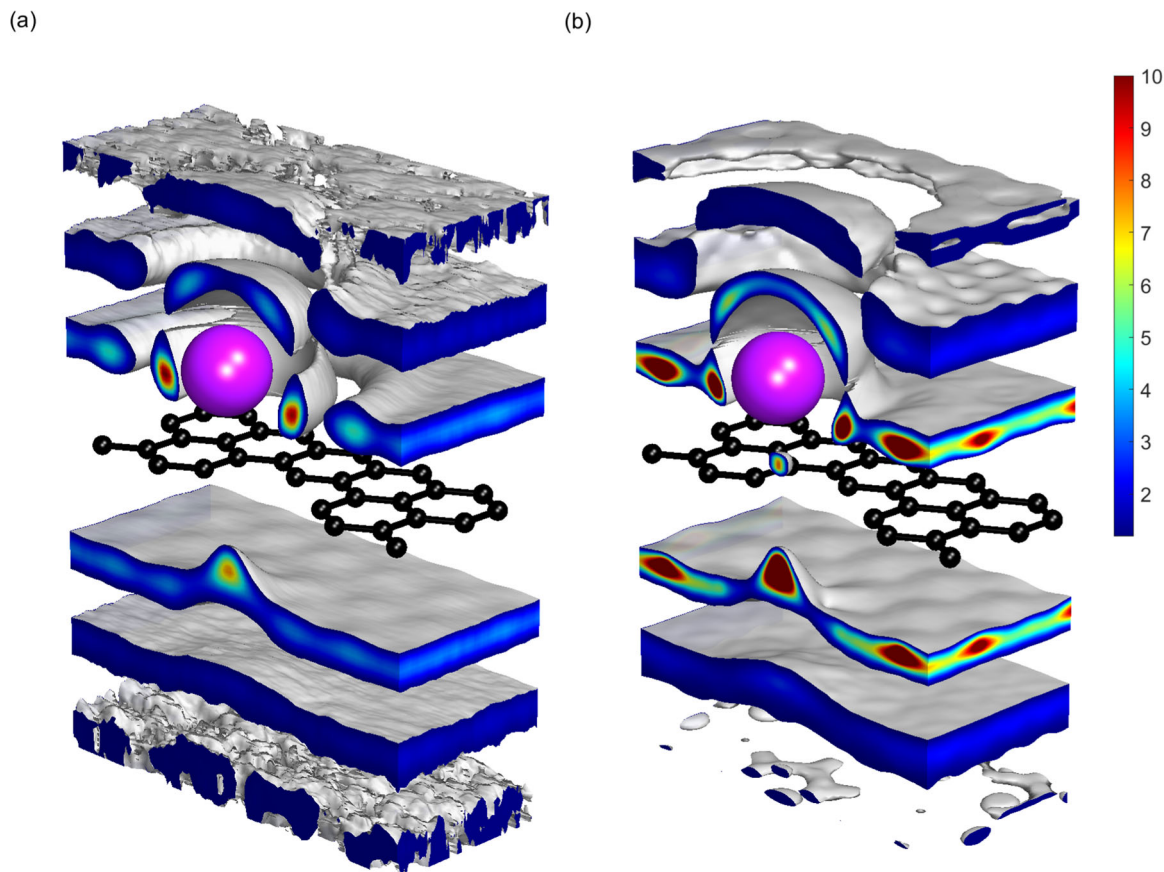


**Fig. 3 Three-dimensional ionic hydration patterns.** Water distribution around a  $K^+$  ion (purple sphere) at  $Z = 0.4$  nm near the pore in a graphene lattice (black ball-and-stick representation), obtained from **a** MD simulations and **b** theory (Eq. (4)). An isovalue of 1.15 was chosen to reveal the layered structure of the hydration around the ion and the graphene lattice. Both panels have been smoothed with a 5-point window.

designing the function of Angström-scale ionic devices. In Supplementary Discussion 4, we consider a tentative analytical way of connecting the hydration patterns and the single-ion PMF. Below we compare the ionic hydration patterns, obtained from MD simulations, with those from theory (Eq. (4)).

**MD simulation results.** Figure 2 compares the MD results (top row) with the corresponding theoretical predictions, Eq. (4) (middle row). They agree well in that the qualitative features of the water distributions are well reproduced: as described by the  $\Pi g_{iw}$  term in Eq. (4), superposition of the contributions from all the carbon atoms results in a decaying plane density wave in the  $z$ -direction, matching the troughs and peaks of the C–OH RDFs (see Supplementary Fig. 2). The presence of the pore in an otherwise intact lattice distorts the water layers near the membrane and allows water molecules to exist in the pore as revealed by the strength of their distribution.

An ion in the pore (Fig. 2c), suggests spherically symmetric spatial density waves, as implied by the term  $g_{iw}$  in Eq. (4). The resultant superposition of the plane wave from the graphene with the spherically symmetrical hydration shells from the ion leads to a reshaping of the density such that the first hydration shell, while partially remaining, becomes significantly altered. In particular, it acquires maxima where the O–C and O– $K^+$  RDF maxima coincide minima when both RDFs reach minima and mid-values where the maximum of one RDF overlaps with the minimum of another. Circular waves in Fig. 2b, c, e, f around the ion corresponding to the first two maxima of the intact bulk O– $K^+$  RDF, indicated by the concentric circles at their respective radii. The density around the centrally located ion preserves the first

hydration shell, but with a modulation due to the graphene atoms; the structure of the second shell is significantly affected by interactions with carbon atoms. Thus, the observed water patterns arise from interference between the ionic hydration shell and the hydration cloud around the nanopore. Analysis of the hydration patterns around  $Na^+$  and  $Cl^-$  ions, shown in Supplementary Note 1, reveals similar features.

The central parts of Fig. 2b, e are shown at higher resolution in panels (g) and (h). One can see the fine structure in the water density pattern resulting from the superposition of the ion–oxygen and carbon–oxygen interactions. The density crescent at  $Z \approx 0.6$  nm in Fig. 2g, h is induced by the first maximum of the RDF, as indicated by the concentric circles, while the two peaks appear due to the oxygen interaction with the carbon atoms. The low-density area around  $[0.45, \pm 0.25]$  nm emerges due to the minimum of the  $K^+$ –O $^-$  RDF located at around 0.35 nm. The “island” around  $[0.175, 0]$  nm indicates the position of the trapped water molecule, and highlights the predictive power of the proposed analytical method (see Supplementary Note 2 for more details). The cross-sections of the crescents in Fig. 2g, h, made at 0.25 nm, are shown in panels (i) and (j). These arise from an interplay between the oxygen–ion and oxygen–pore interactions: the minimum at the origin arises due to the convex shape of the first hydration shell near the ion, while the hexagonal structure is inherited from the hexagonal geometry of the graphene pore (grey balls and sticks). Similar water density patterns in the plane of the nanopores have been observed in numerous MD simulation works<sup>8,17,18,22,30</sup> recently.

Figure 3 combines the previous results by illustrating the 3D isosurfaces of the hydration shells around the ion and the pore,

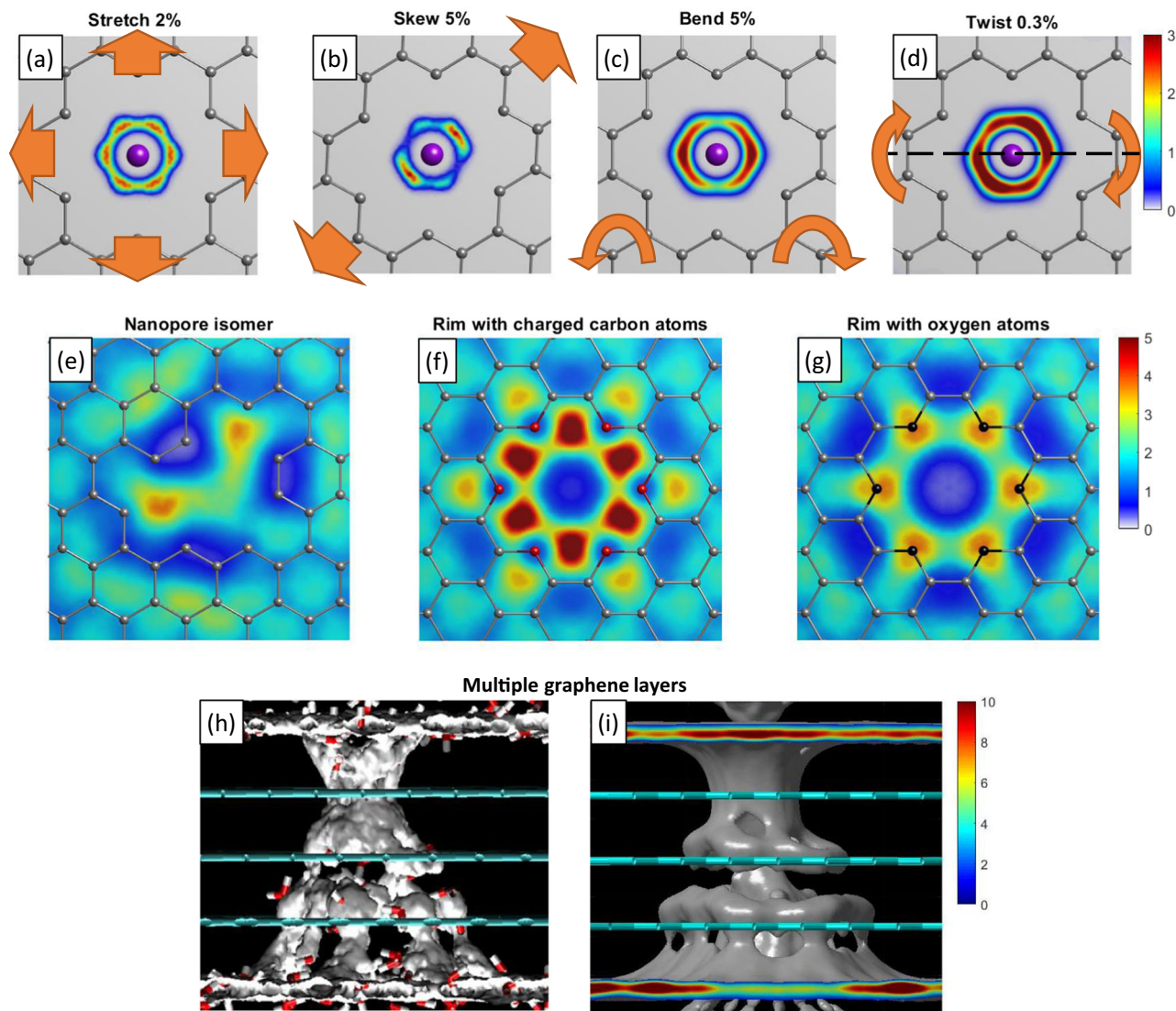


**Fig. 4 Tools to control the hydration pattern.** These include the extrinsic processes of: **a** stretching, **b** skewing or asymmetric stretching, **c** bending, **d** twisting, and the intrinsic features of—**e** choice of pore isomer, **f** charging of the rim atoms (red balls), **g** functionalising the rim with oxygen atoms (black balls), **h** use of a multi-layer pore, as exemplified in a molecular dynamics simulation (**h** adapted from ref. <sup>61</sup>, copyright 2019, with permission from Elsevier), and **i** theoretical prediction, Eq. (4). Density slices have been taken at  $Z = -0.23$  nm (**a**)–(**d**) and  $Z = -0.28$  nm (**e**)–(**g**). The graphene lattice is indicated in a grey ball-and-stick representation.

taken at a level of 1.15. Panels a and b show that the results from MD and theoretical prediction Eq. (4), respectively, agree well. These figures reproduce the layering of water near the graphene sheet, with the first three layers visible (see Supplementary Note 3 for details), as well as the spherical hydration shells around the  $K^+$  ion. Parts of the preserved 1st and 2nd hydration shells are clearly evident. The figure emphasises the inhomogeneity and anisotropy of the water patterns emerging from the combined effects of the ion and the graphene lattice. The origin of multiple water layers is illustrated in Supplementary Fig. 12.

We have also studied how the hydration structure evolves as the ion's position changes. The results are summarised in Supplementary Note 4 and the two Supplementary frame series (Supplementary Movies 1 and 2). These sets clearly illustrate that the water structure is significantly modified, even when the ion is located more than 1 nm away from the nanopore. In other words, when the lattice-induced (hydration layers) and ion-induced (hydration shells) inhomogeneities begin to overlap, the ion–pore interaction starts to change. This result supports the notion that

solvent-mediated interactions extend the range of the interactions with the pore by a large factor compared with the bare ion radius<sup>60</sup>.

Finally, in Fig. 4 we illustrate the predicted effects of the set of tools that we propose for controlling the dehydration pattern. They can be categorised into two groups. The first set is extrinsic and includes (a) stretching, (b) skewing or asymmetrical stretching, (c) bending, and (d) twisting of the lattice (see Supplementary Notes 8–11). Secondly, we propose adjustments of some intrinsic features: (e) the nanopore geometry, (f) rim charge, (g) atom type and (i) layer number (see Supplementary Notes 12–17). Our theory yields good agreement with the published crown-like water density patterns (panel (h)) from ref. <sup>61</sup>. More examples of these tools in action are given in Section 3 of the Supplementary Information.

It is evident that Eq. (4) can reproduce well the qualitative features of the water distribution near the pore given in Fig. 2. We point out, however, that there is a numerical discrepancy—a factor of  $\sim 3$ —between the peak values of the maps, clearly seen

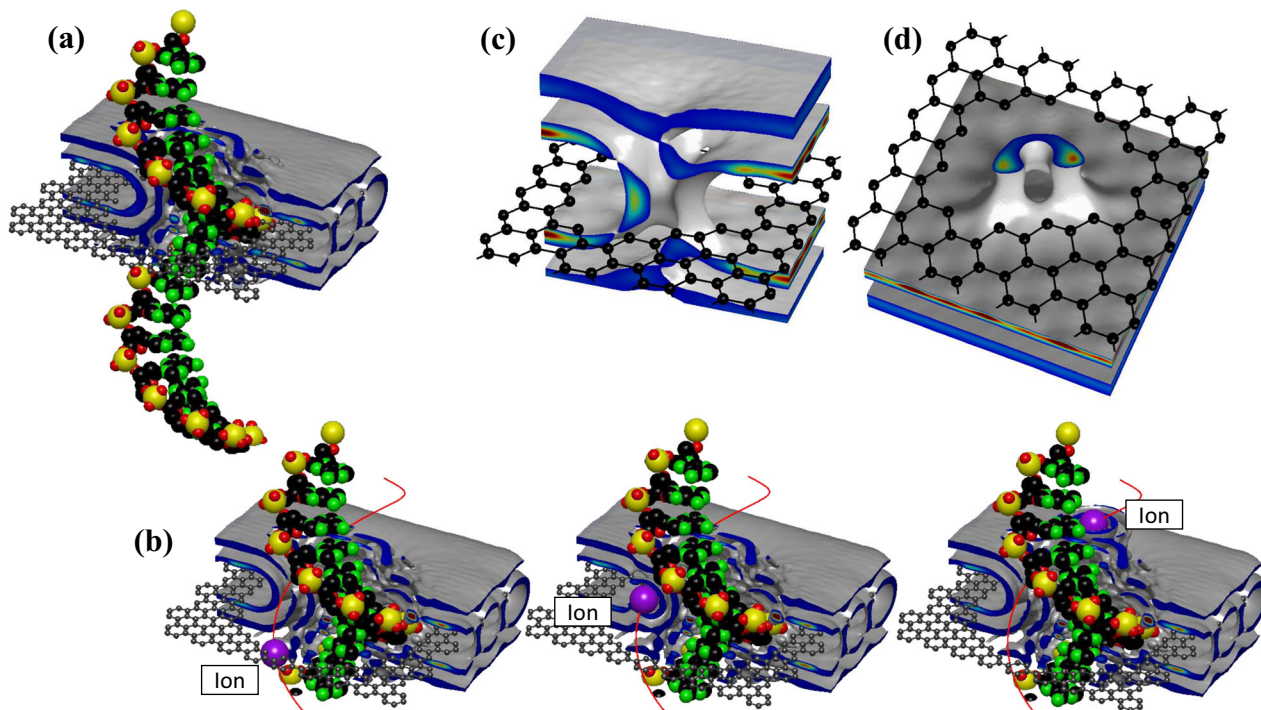


**Fig. 5 Possible applications of our proposed method to DNA sequencing and the cataloguing of the solvated nanopore isomers.** **a** Hydration pattern wetting the single-stranded DNA in a nanopore. Densities are obtained from Eq. (4) and are shown as grey isosurfaces (isovalued = 1.2) and coloured cross-sections. The DNA is represented by connected coloured spheres (oxygen (red), nitrogen (green), carbon (black), phosphorus (yellow)). Graphene lattice is shown in grey balls and sticks. **b** Three consecutive snapshots of the K<sup>+</sup> ionic trajectory along the groove of the DNA, depicted by the red line. **c, d** Represent the nontrivial structure of the solvation patterns around one of the pore isomers, taken from ref. <sup>78</sup> (isomer for the case of  $N = 19$ , the frequency of observation of the isomer—4%—total number of possible isomers—488<sup>78</sup>). The isosurfaces are calculated at the isovalued of 1.2. Graphene lattice is shown in black balls and sticks.

between the MD-generated and theoretical density of the “ridges” near the graphene lattice. We attribute this discrepancy to our omission of the water–water interactions in Eq. (4), which would imply an absence of short-range repulsion between oxygen or hydrogen atoms of separate water molecules, so that arbitrarily small separations can be realised. The consequence is denser water distribution, localised near the carbon atoms. Also, the reduction from a full 3D model to the radial CF picture overlooks the water–water relative orientations and thus limits the applicability of the method in carbon nanotubes. We are currently working on eliminating these shortcomings of the technique by using higher-dimensional CFs<sup>50</sup> and applying machine learning (see Supplementary Discussion 5 for a toy example).

## Discussion

Our approach can readily be extended to account for the density of hydrogen atoms, and thus to evaluate the average charge density in the domain. Doing so promises deep insight into water-mediated interactions, including the pore rim’s hydration<sup>62</sup> and reorientation of the water dipoles in confinement which reduces<sup>63,64</sup> the dielectric permittivity. The latter is needed for quantifying the ion and polymer interactions with the pore and with the external electric field and for understanding the ionic diffusivity<sup>65</sup> in biological channels, as well as the properties of the electric double layer<sup>66,67</sup>. The method can also be used to define the demarcation interface between the pore and the protein in continuous theories of ion transport such as the Poisson–Nernst–Planck (PNP) theory<sup>68</sup>. The method can thus provide fundamental insights into the electrostatics and dynamics

of ions in sub-nanopores, where the dielectric properties on the nanoscale remain a challenging unsolved problem that is subject to intensive research<sup>35,36,69,70</sup>.

Our results demonstrate the applicability of the method to describing water density patterns under quite general conditions, e.g. for arbitrary ionic positions, pore geometry (size, shape, number of layers, offset eclipse<sup>71</sup>), stretching, skewing, bending, and twisting of the lattice, the type of atom around the rim of the pore, and the nature of the 2D material<sup>72</sup>. This opens the way to multi-parameter optimisation<sup>73</sup> of the energy landscape by adjustment of the corresponding hydration patterns. For example, by iteratively choosing the most appropriate combination of pore geometric parameters, and subsequently manipulating the pore shape externally (e.g. by stretching), the nanopore’s permeability and selectivity can be optimised and regulated, providing for permeation along specified pathways<sup>74–76</sup>. This approach could prove useful in addressing two highly topical technological challenges: first, water desalination, to maximise the quality and energy efficiency while minimising the environmental impact of the process<sup>7</sup>; and secondly, energy harvesting, to maximise energy conversion by minimising Joule heating, thereby raising the output power density above the level of 5 W/m<sup>2</sup> needed to make harvesting economically viable<sup>12,14</sup>.

The same design and optimisation strategy should serve to slow down the translocation and guide the orientation of DNA (see Fig. 5a for a possible example), which constitutes one of the current challenges to fast genome sequencing<sup>11,77</sup>. Likewise, it is believed that the accuracy of nucleobase detection using the Coulter principle can benefit from an optimisation of the features of the nanopore, Fig. 5b (see also Supplementary Movies 3, 4, and Note 5). Our approach would allow one to catalogue solvated 2D

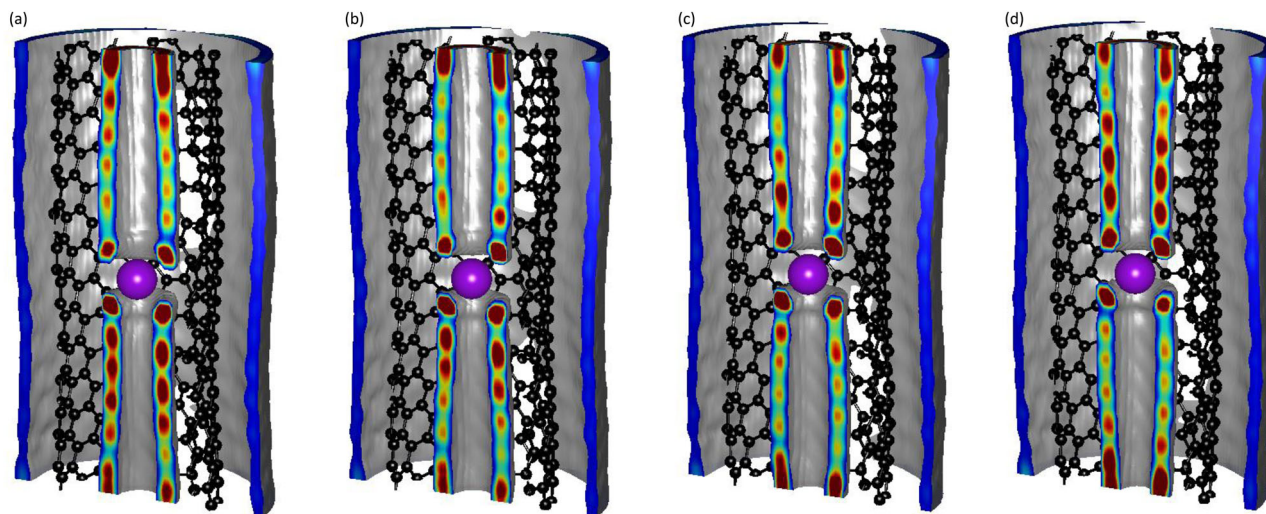


**Fig. 6** Water density patterns in a (5,10) CNT with a mechanical wave travelling along with it. Panels a–d show frames taken at intervals  $t_m = (\frac{0}{6}, \frac{1}{6}, \frac{2}{6}, \frac{3}{6})T$ , where  $T$  is the period of the wave. This provides an illustration of how a transverse wave, travelling along the CNT axis, may lead to the directed motion of ions against the electrochemical gradient, thus providing a potential design for mechanically induced ion-pumping. See Supplementary Movie 5 for a visualisation.

and 3D pore isomers<sup>78</sup>, as illustrated in Fig. 5c, d, thus benefiting the Materials Genome Initiative<sup>79,80</sup>. Finally, by applying a travelling transverse (corrugated) wave one might be able to create a nanoscale ionic pump driving ions against the electrochemical gradient<sup>81</sup> (see Fig. 6, Supplementary Movie 5 and Note 6). Thus, the proposed method paves the way to the optimisation and design of novel nanoionic devices in many contexts and applications<sup>82</sup>.

## Conclusions

We have proposed and validated an analytic method for revealing and quantifying the hydration patterns around an ion near a sub-nanopore, using a product of the RDFs measured in the bulk electrolyte. The complexity and fragmentation of these patterns result from interference between ionic hydration shells and the hydration cloud around the nanopore. The method can be extended to account for the distribution of hydrogen atoms, and hence to obtain insight into local electrostatic interactions on the nanoscale. It is fast, and it allows one to take explicit account of the nanopore's detailed geometry (size, length, shape, number of layers, offset eclipse), pore constituents (charge and atom type), and of the ion's position, as well as implicitly to take account of the ion type, solvent, temperature, and pressure. Multi-parameter optimisation of the pore parameters and surroundings is expected to create a way of engineering and regulating the energy barrier in nanopores via control of the hydration pattern. This strategy opens a new avenue to designing, optimising, and controlling the permeability and selectivity properties of nanoionic devices, as well as regulating the translocation of DNA through solid-state nanopore sequencers.

## Methods

**MD simulation details.** We used VMD<sup>83</sup> to build the systems in question, and NAMD2<sup>84</sup> with the CHARMM27 force field for MD simulations at  $T = 300$  K with a time step of 1 fs and the velocity Verlet algorithm. The Lorentz–Berthelot combining rule was applied. The TIP3P<sup>85</sup> water model was used. A cutoff of 1.2 nm for non-bonded interactions (Lennard–Jones and Coulomb) with a switching distance of 10.0 Å (1 nm) was used, and the full electrostatic calculation was performed using the particle mesh Ewald (PME) scheme<sup>86</sup>. Periodic boundary conditions were imposed in all directions.

All lattice atoms were fixed by setting the `beta` parameter to 1. The system first underwent equilibration during the initial 1000 steps in the Nosé–Hoover

thermostat at pressure  $p = 1$  atm (101.325 kPa), with the remaining simulation running under NVT conditions. The frames were captured every 100 steps. No external electric field was applied. Unless otherwise stated, typical production runs took 10 ns and were sampled every 100 steps to yield statistically significant figures.

RDFs were measured for a free atom (C,  $K^+$ ,  $Na^+$ ) in the water surroundings. When an ion's RDF was measured, the corresponding number of free counterions ( $Cl^-$  for  $K^+$ , and  $K^+$  for  $Cl^-$ ) was added to neutralise the system. Finally, RDFs were measured using the VMD plugin `gofr`. Molecular structures were visualised and rendered using VMD<sup>83</sup>.

**Data analysis.** MD trajectories were read by a `readddc.m` and `readpdb.m` scripts `MDToolbox`<sup>87</sup> for MATLAB<sup>88</sup>. A homemade script to build and analyse the histogram distributions included built-in MATLAB functions and some external functions: `histcn.m`<sup>89</sup>, `smooth2a.m`<sup>90</sup>. All densities were normalised by the bulk values. A  $3 \times 3$ -point smoothing window was applied to suppress the pixelation of the MD histograms, unless otherwise stated.

## Data availability

The datasets generated during and/or analysed during the current study are available from the corresponding author on reasonable request.

## Code availability

MATLAB codes for computing the ionic hydration patterns according to Eq. (4) and creating a movie analogous to Supplementary Movie 2, and transforming the crystal lattice are available as ZIP archives in Supplementary Data 1 and 2 (see Supplementary Note 7 for details). Other codes that support the results reported in this paper and other findings of this study are available from the corresponding author upon reasonable request.

Received: 15 March 2021; Accepted: 6 May 2021;

Published online: 18 June 2021

## References

- Bond, A. H., Dietz, M. L. & Chiarizia, R. Incorporating size selectivity into synergistic solvent extraction: a review of crown ether-containing systems. *Ind. Eng. Chem. Res.* **39**, 3442–3464 (2000).
- Faucher, S. et al. Critical knowledge gaps in mass transport through single-digit nanopores: a review and perspective. *J. Phys. Chem. C* **123**, 21309–21326 (2019).
- Wang, Y., Chen, K. S., Mishler, J., Cho, S. C. & Adroher, X. C. A review of polymer electrolyte membrane fuel cells: technology, applications, and needs on fundamental research. *Appl. Energy* **88**, 981–1007 (2011).

4. Hille, B. *Ion Channels of Excitable Membranes* 3rd edn (Sinauer Associates Inc, 2001).
5. Cohen-Tanugi, D. & Grossman, J. C. Water desalination across nanoporous graphene. *Nano Lett.* **12**, 3602–3608 (2012).
6. Rollings, R. C., Kuan, J. A. & Golovchenko, A. T. Ion selectivity of graphene nanopores. *Nat. Commun.* **7**, 11408 (2016).
7. Lee, A., Elam, J. W. & Darling, S. B. Membrane materials for water purification: design, development, and application. *Environ. Sci.* **2**, 17–42 (2016).
8. Fang, A., Kroenlein, K., Riccardi, D. & Smolyanitsky, A. Highly mechanosensitive ion channels from graphene-embedded crown ethers. *Nat. Mater.* **18**, 76–81 (2019).
9. Du, H. et al. Separation of hydrogen and nitrogen gases with porous graphene membrane. *J. Phys. Chem. C* **115**, 23261–23266 (2011).
10. Lozada-Hidalgo, M. et al. Sieving hydrogen isotopes through two-dimensional crystals. *Science* **351**, 68–70 (2016).
11. Heerema, S. J. & Dekker, C. Graphene nanodevices for DNA sequencing. *Nat. Nanotechnol.* **11**, 127–136 (2016).
12. Graf, M., Lihter, M., Altus, D., Marion, S. & Radenovic, A. Transverse detection of DNA using a MoS<sub>2</sub> nanopore. *Nano Lett.* **19**, 9075–9083 (2019).
13. Liu, G., Chen, T., Xu, J. & Wang, K. Blue energy harvesting on nanostructured carbon materials. *J. Mater. Chem. A* **6**, 18357–18377 (2018).
14. Macha, M., Marion, S., Nandigana, V. V. R. & Radenovic, A. 2D materials as an emerging platform for nanopore-based power generation. *Nat. Rev. Mater.* **4**, 588–605 (2019).
15. Joshi, R. K. et al. Precise and ultrafast molecular sieving through graphene oxide membranes. *Science* **343**, 752–754 (2014).
16. Esfandiari, A. et al. Size effect in ion transport through Angstrom-scale slits. *Science* **358**, 511–513 (2017).
17. Fang, A., Kroenlein, K. & Smolyanitsky, A. Mechanosensitive ion permeation across subnanoporous MoS<sub>2</sub> monolayers. *J. Phys. Chem. C* **123**, 3588–3593 (2019).
18. Zwolak, M., Lagerqvist, J. & Di Ventra, M. Quantized ionic conductance in nanopores. *Phys. Rev. Lett.* **103**, 128102 (2009).
19. Kaufman, I., Luchinsky, D. G., Tindjong, R., McClintock, P. V. E. & Eisenberg, R. S. Energetics of discrete selectivity bands and mutation-induced transitions in the calcium–sodium ion channels family. *Phys. Rev. E* **88**, 052712 (2013).
20. Kaufman, I. K., McClintock, P. V. E. & Eisenberg, R. S. Coulomb blockade model of permeation and selectivity in biological ion channels. *New J. Phys.* **17**, 083021 (2015).
21. Kaufman, I. K. & McClintock, P. V. E. Ionic Coulomb blockade. *Nat. Mater.* **15**, 825–826 (2016).
22. Sahu, S., Di Ventra, M. & Zwolak, M. Dehydration as a universal mechanism for ion selectivity in graphene and other atomically thin pores. *Nano Lett.* **17**, 4719–4724 (2017).
23. Guardiani, C., Fedorenko, O. A., Khovanov, I. A. & Roberts, S. K. Different roles for aspartates and glutamates for cation permeation in bacterial sodium channels. *Biochim. Biophys. Acta Biomembr.* **1861**, 495–503 (2019).
24. Guardiani, C., Gibby, W. A. T., Barabash, M. L., Luchinsky, D. G. & McClintock, P. V. E. Exploring the pore charge dependence of K<sup>+</sup> and Cl<sup>−</sup> permeation across a graphene monolayer: a molecular dynamics study. *RSC Adv.* **9**, 20402–20414 (2019).
25. Gibby, W. A. T., Barabash, M. L., Guardiani, C., Luchinsky, D. G. & McClintock, P. V. E. The role of noise in determining selective ionic conduction through nano-pores. In *2018 IEEE 13th Nanotechnology Materials and Devices Conference (NMDC)* (IEEE, 2019).
26. Zhan, H. et al. Solvation-involved nanoionics: new opportunities from 2D nanomaterial laminar membranes. *Adv. Mater.* **32**, 1904562 (2020).
27. Smolyanitsky, A., Fang, A., Kazakov, A. F. & Paulechka, E. Ion transport across solid-state ion channels perturbed by directed strain. *Nanoscale* **12**, 10328–10334 (2020).
28. Fedorenko, O. A. et al. Ionic Coulomb blockade and the determinants of selectivity in the NaChBac bacterial sodium channel. *Biochim. Biophys. Acta Biomembr.* **1862**, 183301 (2020).
29. Zwolak, M., Wilson, J. & Ventra, M. D. Dehydration and ionic conductance quantization in nanopores. *J. Phys.: Condens. Matter* **22**, 454126 (2010).
30. Gao, H., Shi, Q., Král, P. & Lu, R. Water transport through ultrathin nanopores with highly polar rims. *J. Phys. Chem. C* **123**, 27690–27696 (2019).
31. Zhang, X., Wei, M., Xu, F. & Wang, Y. Thickness-dependent ion rejection in nanopores. *J. Membr. Sci.* **601**, 117899 (2020).
32. Akaishi, A., Yonemaru, T. & Nakamura, J. Formation of water layers on graphene surfaces. *ACS Omega* **2**, 2184–2190 (2017).
33. Mendonça, B. H. et al. Diffusion behaviour of water confined in deformed carbon nanotubes. *Physica A* **517**, 491–498 (2019).
34. Chen, B., Jiang, H., Liu, X. & Hu, X. Molecular insight into water desalination across multilayer graphene oxide membranes. *ACS Appl. Mater. Interfaces* **9**, 22826–22836 (2017).
35. Ballenegger, V. & Hansen, J.-P. Dielectric permittivity profiles of confined polar fluids. *J. Chem. Phys.* **122**, 114711 (2005).
36. Bonthuis, D. J., Gekle, S. & Netz, R. R. Profile of the static permittivity tensor of water at interfaces: consequences for capacitance, hydration interaction and ion adsorption. *Langmuir* **28**, 7679–7694 (2012).
37. Rigo, E. et al. Measurements of the size and correlations between ions using an electrolytic point contact. *Nat. Commun.* **10**, 2382 (2019).
38. Gibby, W. A. T. et al. Theory and experiments on multi-ion permeation and selectivity in the NaChBac ion channel. *Fluct. Noise Lett.* **18**, 1940007 (2019).
39. Barabash, M. L., Gibby, W. A. T., Guardiani, C., Luchinsky, D. G. & McClintock, P. V. E. From the potential of the mean force to a quasiparticle's effective potential in narrow ion channels. *Fluct. Noise Lett.* **18**, 1940006 (2019).
40. Ruan, Y. et al. Molecular dynamics study of Mg<sup>2+</sup>/Li<sup>+</sup> separation via biomimetic graphene-based nanopores: the role of dehydration in second shell. *Langmuir* **32**, 13778–13786 (2016).
41. Wang, Z.-Y. & Wu, J. Ion association at discretely-charged dielectric interfaces: giant charge inversion. *J. Chem. Phys.* **147**, 024703 (2017).
42. Amiri, H., Shepard, K. L., Nuckolls, C. & Hernández Sánchez, R. Single-walled carbon nanotubes: mimics of biological ion channels. *Nano Lett.* **17**, 1204–1211 (2017).
43. Novoselov, K. S. et al. Electric field effect in atomically thin carbon films. *Science* **306**, 666–669 (2004).
44. Kirkwood, J. G. & Boggs, E. M. The radial distribution function in liquids. *J. Chem. Phys.* **10**, 394–402 (1942).
45. Allen, M. P. & Tildesley, D. J. *Computer Simulation of Liquids* (Clarendon Press, 1987).
46. McQuarrie, D. M. *Statistical Mechanics* (University Science Books, 2000).
47. Ben-Naim, A. *Molecular Theory of Solutions* (OUP Oxford, 2006).
48. Egwolf, B., Luo, Y., Walters, D. E. & Roux, B. Ion selectivity of  $\alpha$ -hemolysin with  $\beta$ -cyclodextrin adapter. ii. Multi-ion effects studied with grand canonical Monte Carlo/Brownian dynamics simulations. *J. Phys. Chem. B* **114**, 2901–2909 (2010).
49. Comer, J. & Aksimentiev, A. Predicting the DNA sequence dependence of nanopore ion current using atomic-resolution Brownian dynamics. *J. Phys. Chem. C* **116**, 3376–3393 (2012).
50. Hummer, G. & Soumpasis, D. M. Computation of the water density distribution at the ice-water interface using the potentials-of-mean-force expansion. *Phys. Rev. E* **49**, 591–596 (1994).
51. Kirkwood, J. G. Statistical mechanics of fluid mixtures. *J. Chem. Phys.* **3**, 300–313 (1935).
52. Gray, C. G. & Gubbins, K. E. *Theory of Molecular Fluids* (Oxford University Press, 1984).
53. Hummer, G., García, A. & Soumpasis, D. Hydration of nucleic acid fragments: comparison of theory and experiment for high-resolution crystal structures of RNA, DNA, and DNA–drug complexes. *Biophys. J.* **68**, 1639–1652 (1995).
54. Soper, A. K. The radial distribution functions of water as derived from radiation total scattering experiments: is there anything we can say for sure? *ISRN Phys. Chem.* **2013**, 67 (2013).
55. Clayton, G. T. & Heaton, L. Neutron diffraction study of krypton in the liquid state. *Phys. Rev.* **121**, 649–653 (1961).
56. Feig, M. *Modeling Solvent Environments: Applications to Simulations of Biomolecules* (Wiley-VCH Verlag GmbH & Co. KGaA, 2010).
57. Hirata, F. *Molecular Theory of Solvation* (Kluwer Academic Publishers, 2004).
58. Hansen, J. P. & McDonald, I. R. *Theory of Simple Liquids* (Academic Press Inc. (London) Ltd., 1976).
59. Beglov, D. & Roux, B. An integral equation to describe the solvation of polar molecules in liquid water. *J. Phys. Chem. B* **101**, 7821–7826 (1997).
60. Beckstein, O., Tai, K. & Sansom, M. S. P. Not ions alone: barriers to ion permeation in nanopores and channels. *J. Am. Chem. Soc.* **126**, 14694–14695 (2004).
61. Jhon, Y. I., Kim, C., Byun, Y. T., Lee, J. H. & Jhon, Y. M. Facile large-area fabrication of highly selective and permeable few-layered graphene: a molecular dynamics study. *Carbon* **155**, 369–378 (2019).
62. Barabash, M. et al. Field-dependent dehydration and optimal ionic escape paths for C<sub>2</sub>N membranes. *J. Phys. Chem. C* (2021) (in revision).
63. Gongadze, E. & Igljić, A. Asymmetric size of ions and orientational ordering of water dipoles in electric double layer model—an analytical mean-field approach. *Electrochim. Acta* **178**, 541–545 (2015).
64. Fumagalli, L. et al. Anomalous low dielectric constant of confined water. *Science* **360**, 1339–1342 (2018).
65. Roux, B., Allen, T., Berneche, S. & Im, W. Theoretical and computational models of biological ion channels. *Q. Rev. Biophys.* **37**, 15–103 (2004).
66. Schoch, R. B., Han, J. & Renaud, P. Transport phenomena in nanofluidics. *Rev. Mod. Phys.* **80**, 839–883 (2008).
67. Gillespie, D., Petsev, D. N. & van Swol, F. Electric double layers with surface charge regulation using density functional theory. *Entropy* **22**, 132 (2020).



68. Eisenberg, B., Hyon, Y. & Liu, C. Energy variational analysis of ions in water and channels: field theory for primitive models of complex ionic fluids. *J. Chem. Phys.* **133**, (2010).
69. Sato, T., Sasaki, T., Ohnuki, J., Umezawa, K. & Takano, M. Hydrophobic surface enhances electrostatic interaction in water. *Phys. Rev. Lett.* **121**, 206002 (2018).
70. Varghese, S., Kannam, S. K., Hansen, J. S. & P. Sathian, S. Effect of hydrogen bonds on the dielectric properties of interfacial water. *Langmuir* **35**, 8159–8166 (2019).
71. Zhou, W., Wei, M., Zhang, X., Xu, F. & Wang, Y. Fast desalination by multilayered covalent organic framework (cof) nanosheets. *ACS Appl. Mater. Interfaces* **11**, 16847–16854 (2019).
72. Sui, X., Yuan, Z., Yu, Y., Goh, K. & Chen, Y. 2D material based advanced membranes for separations in organic solvents. *Small* **16**, 2003400 (2020).
73. Nocedal, J. & Wright, S. J. *Numerical Optimization. Springer series in Operations Research* 2nd edn (Springer, 2006).
74. Dykman, M. I., Luchinsky, D. G., McClintock, P. V. E. & Smelyanskiy, V. N. Coralls and critical behavior of the distribution of fluctuational paths. *Phys. Rev. Lett.* **77**, 5229–5232 (1996).
75. Luchinsky, D. G. & McClintock, P. V. E. Irreversibility of classical fluctuations studied in analogue electrical circuits. *Nature* **389**, 463–466 (1997).
76. Guardiani, C. et al. Prehistory probability distribution of ionic transitions through a graphene nanopore. In *Proceedings of the 25th International Conference on Noise and Fluctuations (ICNF) (eds Enz, C. & Pascal, F.)* (EPFL, 2019).
77. Yuan, Z., Liu, Y., Dai, M., Yi, X. & Wang, C. Controlling DNA translocation through solid-state nanopores. *Nanoscale Res. Lett.* **15** <https://doi.org/10.1186/s11671-020-03308-x> (2020).
78. Rajan, G. A. et al. Addressing the isomer cataloguing problem for nanopores in two-dimensional materials. *Nat. Mater.* **18**, 129–135 (2019).
79. Materials Genome Initiative, (accessed 18 May 2021) <https://www.nist.gov/mgi>.
80. de Pablo, J. J. et al. New frontiers for the materials genome initiative. *Npj Comput. Mater.* **5** <https://doi.org/10.1038/s41524-019-0173-4> (2019).
81. Marbach, S., Dean, D. S. & Bocquet, L. Transport and dispersion across wiggling nanopores. *Nat. Phys.* **14**, 1108–1113 (2018).
82. Epsztein, R., DuChanois, R. M., Ritt, C. L., Noy, A. & Elimelech, M. Towards single-species selectivity of membranes with subnanometre pores. *Nat. Nanotechnol.* <http://www.nature.com/articles/s41565-020-0713-6> (2020).
83. Humphrey, W., Dalke, A. & Schulten, K. VMD: visual molecular dynamics. *J. Mol. Graph.* **14**, 33–38 (1996).
84. Phillips, J. C. et al. Scalable molecular dynamics with NAMD. *J. Comput. Chem.* **26**, 1781–1802 (2005).
85. Jorgensen, W. L., Chandrasekhar, J., Madura, J. D., Impey, R. W. & Klein, M. L. Comparison of simple potential functions for simulating liquid water. *J. Chem. Phys.* **79**, 926–935 (1983).
86. Essmann, U. et al. A smooth particle mesh Ewald method. *J. Chem. Phys.* **103**, 8577–8593 (1995).
87. Matsunaga, Y. *MDToolbox* <https://github.com/ymatsunaga/mdtoolbox> (2018).
88. *MATLAB*, 9.8.0.1538580 (R2020a). Natick, Massachusetts: The MathWorks Inc. <https://www.mathworks.com> (2020).
89. Luong, B. *N-dimensional Histogram* <https://uk.mathworks.com/matlabcentral/fileexchange/23897-n-dimensional-histogram> (2011).
90. Reeves, G. *smooth2a* <https://uk.mathworks.com/matlabcentral/fileexchange/23287-smooth2a> (2009).

## Acknowledgements

We are grateful to N.D. Drummond, B. Luan, A. Stefanovska and N.G. Stocks for valuable discussions. The work was partially supported by a Ph.D. Scholarship from the Faculty of Science and Technology of Lancaster University, by the Engineering and Physical Sciences Research Council UK (grants EP/M016889/1 and EP/M015831/1), and by a Leverhulme Trust Research Project Grant RPG-2017-134. C.G. is currently supported by a project that has received funding from the European Research Council (ERC) under the European Union's Horizon 2020 research and innovation programme (grant agreement No. 803213). M.L.B., C.G., W.A.T.G., D.G.L. and P.V.E.McC gratefully acknowledge the use of the High End Computing facility at Lancaster University. A.S. gratefully acknowledges support from the Materials Genome Initiative. Certain commercial equipment, instruments, or materials are identified in this paper in order to specify the experimental procedure adequately. Such identification is not intended to imply recommendation or endorsement by NIST, nor is it intended to imply that the materials or equipment identified are necessarily the best available for the purpose.

## Author contributions

M.B., A.S. and D.L. conceived the central ideas. M.B. developed the theory, devised and implemented the analysis software. M.B., D.L., W.G. and at the early stage C.G. designed and performed MD simulations. P.V.E.McC. oversaw the project, discussed the results, and helped with the manuscript. All authors discussed the results, contributed to the writing and editing of the manuscript, and approved the final version.

## Competing interests

The authors declare no competing interests.

## Additional information

**Supplementary information** The online version contains supplementary material available at <https://doi.org/10.1038/s43246-021-00162-x>.

**Correspondence** and requests for materials should be addressed to M.L.B.

**Peer review information** Primary handling editor: John Plummer.

**Reprints and permission information** is available at <http://www.nature.com/reprints>

**Publisher's note** Springer Nature remains neutral with regard to jurisdictional claims in published maps and institutional affiliations.



**Open Access** This article is licensed under a Creative Commons Attribution 4.0 International License, which permits use, sharing, adaptation, distribution and reproduction in any medium or format, as long as you give appropriate credit to the original author(s) and the source, provide a link to the Creative Commons license, and indicate if changes were made. The images or other third party material in this article are included in the article's Creative Commons license, unless indicated otherwise in a credit line to the material. If material is not included in the article's Creative Commons license and your intended use is not permitted by statutory regulation or exceeds the permitted use, you will need to obtain permission directly from the copyright holder. To view a copy of this license, visit <http://creativecommons.org/licenses/by/4.0/>.

© The Author(s) 2021